



ISTITUTO NAZIONALE DI RICERCA METROLOGICA Repository Istituzionale

Orthopedic implants affect the electric field induced by switching gradients in MRI

Original

Orthopedic implants affect the electric field induced by switching gradients in MRI / Zilberti, Luca; Arduino, Alessandro; Torchio, Riccardo; Zanovello, Umberto; Baruffaldi, Fabio; Sanchez-lopez, Hector; Bettini, Paolo; Alotto, Piergiorgio; Chiampi, Mario; Bottauscio, Oriano. - In: MAGNETIC RESONANCE IN MEDICINE. - ISSN 0740-3194. - 91:1(2024), pp. 398-412. [10.1002/mrm.29861]

Availability:

This version is available at: 11696/78859 since: 2024-02-19T10:42:07Z

Publisher:

WILEY

Published

DOI:10.1002/mrm.29861

Terms of use:

This article is made available under terms and conditions as specified in the corresponding bibliographic description in the repository

Publisher copyright

WILEY






-

(Article begins on next page)

RESEARCH ARTICLE

Magnetic Resonance in Medicine

Orthopedic implants affect the electric field induced by switching gradients in MRI

Luca Zilberti¹  | Alessandro Arduino¹  | Riccardo Torchio²  | Umberto Zanollo¹  | Fabio Baruffaldi³ | Hector Sanchez-Lopez⁴ | Paolo Bettini² | Piergiorgio Alotto² | Mario Chiampi¹ | Oriano Bottauscio¹ 

¹Istituto Nazionale di Ricerca Metrologica (INRIM), Torino, Italy

²Department of Industrial Engineering, Università degli Studi di Padova, Padova, Italy

³IRCCS Istituto Ortopedico Rizzoli, Bologna, Italy

⁴Research Center for Medical Artificial Intelligence, Shenzhen Institute of Advanced Technology, Chinese Academy of Sciences, Shenzhen, Guangdong China

Correspondence

Luca Zilberti, Istituto Nazionale di Ricerca Metrologica, Strada delle Cacce 91, I-10135, Torino, Italy.
Email: l.zilberti@inrim.it

Funding information

European Metrology Programme for Innovation and Research, Grant/Award Number: 17IND01 MIMAS; European Partnership on Metrology, Grant/Award Number: 21NRM05 STASIS

Abstract

Purpose: To investigate whether the risk of peripheral nerve stimulation increases in the presence of bulky metallic prostheses implanted in a patient's body.

Methods: A computational tool was used to calculate the electric field (E-field) induced in a realistic human model due to the action of gradient fields. The calculations were performed both on the original version of the anatomical model and on a version modified through “virtual surgery” to incorporate knee, hip, and shoulder prostheses. Five exam positions within a body gradient coil and one position using a head gradient coil were simulated, subjecting the human model to the readout gradient from an EPI sequence. The induced E-field in models with and without prostheses was compared, focusing on the nerves and all other tissues (both including and excluding the bones from the analysis).

Results: In the nerves, the most pronounced increase in the E-field (+24%) was observed around the knee implant during an abdominal MRI (Y axis readout). When extending the analysis to encompass all tissues (excluding bones), the greatest amplification (+360%) occurred around the knee implant during pelvic MRI (Z axis readout). Notable increases in E-field peaks were also identified around the shoulder and hip implants in multiple scenarios.

Conclusion: Based on the presented results, further investigations aimed at quantifying the threshold of nerve stimulation in the presence of bulky implants are desirable.

KEYWORDS

gradient fields, implants, peripheral nerve stimulation (PNS), safety

1 | INTRODUCTION

In MRI procedures, peripheral nerve stimulation (PNS) refers to the sensation of an activation of the nervous system due to gradient switching. This switching induces an electric field (E-field) in body tissues.¹ PNS is triggered when the E-field surpasses a certain threshold. Depending on its intensity, PNS might become uncomfortable, or even painful,² potentially compromising patient cooperation. The mechanism behind this type of stimulation has been analyzed extensively,³ leading to the development of the standards presented in the International Electrotechnical Commission Standard 60601-2-33.¹ Various aspects of this issue have been investigated in recent years, including the optimal design of coil geometry⁴⁻⁶ and sequences.⁷⁻⁹

The interaction between a metallic object implanted in a patient's body and MRI gradient fields has been analyzed in several papers, specifically dealing with the risk of heating.¹⁰⁻¹⁷ Conversely, the possibility that such an interaction might alter the E-field distribution in native tissues surrounding the object, and its possible effects on PNS, has received little attention. Some authors published on investigations involving spinal fusion devices,^{18,19} generic active implant electrodes,²⁰ and infusion pumps.^{21,22} However, the problem has not been investigated for large orthopedic implants. This is concerning given the rising number of patients with prostheses who undergo MRI exams.²³⁻²⁵

This study aims to quantify the potential increase in E-field magnitude around some of the most common bulky orthopedic prostheses such as shoulder, hip, and knee implants. These implants introduce a marked discontinuity of electrical conductivity with respect to the native tissues. To achieve this, we have performed several numerical simulations, which describe the interaction between the field produced by standard gradient systems and an anatomical human model that has undergone a "virtual surgery" of prosthetic implants.

2 | METHODS

2.1 | Body model and orthopedic implants

The simulation of patient exposure to gradient fields utilized the Korean female body model, Yoon-sun, (height: 1.52 m, weight: 54.6 kg) belonging to the Virtual Population (Sim4Life, Zurich MedTech, Zurich, Switzerland).²⁶ This model, initially used to calculate the E-field in the absence of implants, is composed of 71 native tissues, which have electrical conductivity values set according to the database of low-frequency conductivities provided by the The Foundation for Research on Information

Technologies in Society Foundation.²⁷ The corresponding human model with orthopedic prostheses was also simulated by integrating CAD models of the following implants into the body model.

- **Knee implant:** This implant, designed for total arthroplasty, is composed of femoral and tibial metallic parts, separated by an insulating liner. The overall size of the implant is 68 mm in the left-right direction, 58 mm in the anteroposterior direction, and 96 mm in the head-foot direction. It was implanted in the left leg.
- **Hip implant:** Also for total arthroplasty, this prosthesis includes a metallic acetabular cup and femoral component (femoral head and stem) separated by a polyethylene liner. This prosthesis, used to replace the left hip joint of the model, has a stem length of 125 mm and a spherical head diameter of 28 mm.
- **Shoulder implant:** The last implant is a fully metallic shoulder prosthesis designed for hemiarthroplasty, composed of a stem connected to a hemispherical head. Implanted in the right shoulder, this prosthesis has a stem length of 105 mm and a head diameter of 40 mm.

The metallic parts of the prostheses are composed of a cobalt-chromium-molybdenum alloy (conductivity: 1.16 MS/m), without porous or ceramic coating. The distance between the three prostheses, implanted together in the same body, is large enough to avoid any mutual electromagnetic interaction (the validity of this assumption has been verified, *a posteriori*, in the results).

The model prostheses were integrated in the correct anatomical positions through a "virtual surgery." Sections of bones (e.g., the head of the femur) that would typically be removed in real surgeries were excised. To maintain model consistency, voids created during the virtual surgery were filled in three different ways. In the first approach (surgery 1), the voids were entirely filled with synovial fluid. Because the conductivity of the synovial fluid is not available in the adopted tissue database,²⁷ the conductivity of the CSF, that is, 1.78 S/m, was used. As with other biological fluids (e.g., bile, plasma, aqueous humor, urine), this is much greater than the conductivity of solid tissues (e.g., bones, fat, muscles). The second approach (surgery 2) replaced the voids with connective tissue (conductivity: 0.37 S/m). A third, simplified version (surgery 3) directly overlaid the three CAD implants on the original body model without manipulating the geometry of the surrounding native tissues.

To perform the numerical computations, the original and the modified versions of the human model were segmented into 0.5 mm cubic voxels. This high resolution ensures an accurate anatomical description.

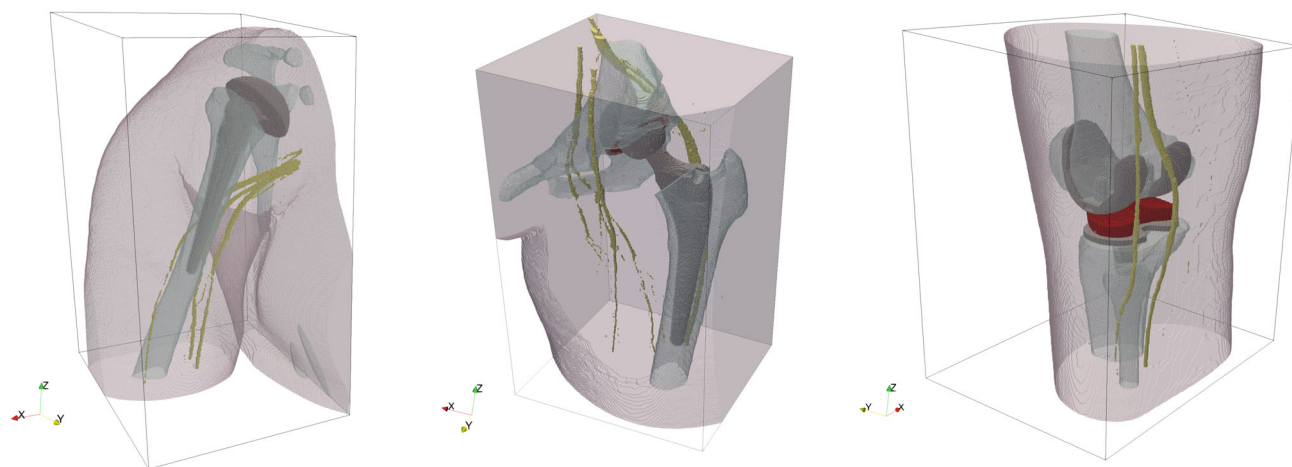


FIGURE 1 The regions investigated, illustrating relative sizes of implants, bones, nerves (yellow), and body contours. Left-to-right: shoulder prosthesis (right shoulder), hip prosthesis (left hip), knee prosthesis (left knee). The hip and knee implants include polyethylene liners (red).

Emphasis was placed on the implants' effects, and E-field analysis was limited to specific regions surrounding the prostheses. The dimensions of these regions ensured that the E-field on their boundaries remained unaffected by the inclusion of the implants. The three implants and corresponding investigation regions are illustrated in Figure 1.

Recent investigations using neurodynamic models²⁸ have shown that large motor nerves are more susceptible to PNS, and a significant (even if not perfect) correlation exists between the location of the peaks of E-field and the location of PNS onset. Given these findings, an analysis of the E-field magnitude induced in the nerves of the human model was conducted. Following the approach recommended by the International Commission on Non-Ionizing Radiation Protection,²⁹ analysis of the induced E-field was also performed in all tissues, assuming the potential presence of small nerves almost everywhere in the body. Because the E-field tends to concentrate in bones (due to the low conductivity), obscuring effects in other tissues, an additional analysis excluding bone tissues (cortical, cancellous, and marrow) was conducted.

2.2 | Gradient systems and gradient signal

A realistic body coil gradient system (internal diameter: 720 mm, axial length: 1500 mm), designed to model a cylindrical MRI scanner, was simulated. The gradient field it produces is compatible with traditional 1.5 T, 3 T, and 7 T MRI scanners.³⁰ An asymmetric, high-performance head gradient coil (internal diameter: 420 mm, axial length: 920 mm), primarily for neuroimaging, was also

considered. Both systems' virtual models were created by discretizing their wires into 1D current-carrying elements, facilitating magnetic field calculations through numerical integration.

For the body gradient coil, five longitudinal positions of the human model (roughly corresponding to MRI exams of the head, thorax, abdomen, pelvis, and femur) were simulated. For each position, the magnitude of the E-field induced in the three investigation regions was recorded. For the head gradient coil, only one position (i.e., MRI at the head) was investigated, limiting the analysis to the region around the shoulder joint (the magnetic field produced by such a coil in the hip and knee regions is almost negligible). Following the standard notation adopted in MRI, the gradient axes will be identified as X (left-right), Y (anteroposterior), and Z (head-foot) for both sets of coils. The positions of the human model with respect to the coils are depicted in Figure 2.

According to the scientific literature, the features of the EPI sequences are particularly relevant concerning PNS. Experimental tests link PNS onset during EPI sequences to the pulse train used in frequency encoding.^{31,32} In addition, the EPI sequence is one of the most popular techniques in functional and diffusion-weighted DWI, useful to perform brain imaging.³³ Thus, in our simulations, the gradient axes were fed with bipolar, symmetric, trapezoidal current waveforms, emulating an EPI sequence's readout signal.

2.3 | Computational approach

To perform the electromagnetic simulations, a recently developed computational approach was adopted.³⁴ This

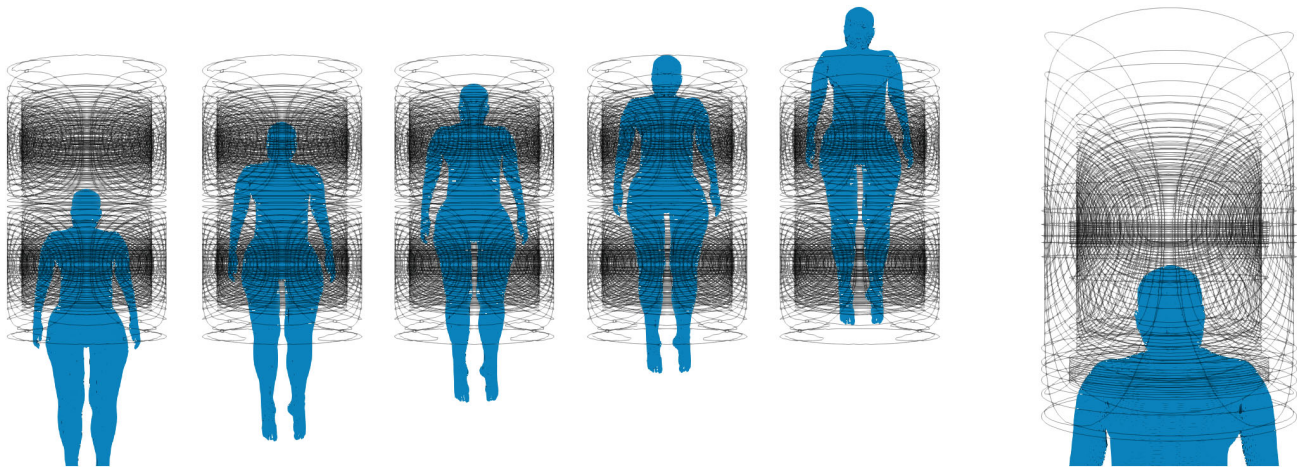


FIGURE 2 Position of the human model with respect to the gradient systems. On the left, the body is placed in five imaging positions (head, thorax, abdomen, pelvis, and femur, respectively) within the body gradient coil. On the right, the head gradient coil is used.

approach belongs to the family of integral formulation methods, which have been used and validated for many large-scale electromagnetic problems in both biomedical³⁵ and nonbiomedical³⁶ applications. The method identifies electric current density and scalar potential as unknown variables. Drawing parallels with the MARIE computational tool,³⁷ this approach exploits the regularity of voxelized human models to minimize computational burden. Moreover, it makes use of model order reduction techniques to expedite time domain analyses.

In principle, the presence of a bulky metallic object, with very high electrical conductivity, might modify the gradient field experienced by the body during a scan. This alteration can be attributed to the eddy currents induced in the metallic components. These currents generate an additional magnetic field that combines with the field generated by the coil, potentially disrupting its spatial distribution and temporal waveform. Consequently, the E-field induced in tissues might diverge from what would be predicted based on an unperturbed gradient magnetic field. To account for this complexity, the adopted computational approach solves the full set of Maxwell's equations (i.e., the total gradient field is an unknown to be determined).

3 | RESULTS

3.1 | Preliminary analysis of the effect of the slew rate

In the biological tissues of the body, without any implant present, the trapezoidal waveform of the gradient field induces rectangular E-field pulses. These pulses are synchronized with the trapezoidal waveform's ramps. The amplitude of these rectangular pulses is proportional to the

slew rate and is not influenced by the duration of intervals between the ramps. However, as mentioned in section 2.3, when implants are present, eddy currents induced in the metallic objects have the potential to modify the gradient field. This could, in turn, distort the E-field pulses induced in the surrounding tissues. To assess the importance of this effect, which gets stronger as the slew rate increases, preliminary simulations were repeated multiple times by increasing the slew rate of the applied gradient field up to 400 (T/m)/s. In these examined cases, the peak magnitudes of the E-field pulses induced in the tissues deviated by less than 1% with respect to the value that would be obtained by disregarding the perturbing effect of the eddy currents.

Given these observations, subsequent results will be presented for a standard unit slew rate of 1 (T/m)/s. A simple linear scaling can be applied to obtain the E-field amplitude relevant to any other slew rate value.

3.2 | Preliminary comparison of the different versions of the virtual surgery

To evaluate the consistency of the results across the different “virtual surgery” modifications made to the Yoon-sun model, some simulations were repeated using each version of the human model with implants. In general, surgeries 1 (CSF used as a filler) and 2 (connective tissue used as a filler) showed highly congruent results. In contrast, the results obtained with surgery 3 (overlap between the CADs of the body and the implants) diverged more significantly from the other two models. An illustrative example is provided in Figure 3. It presents the maximum intensity projection of the E-field magnitude on a coronal plane surrounding the shoulder implant during a head MRI using

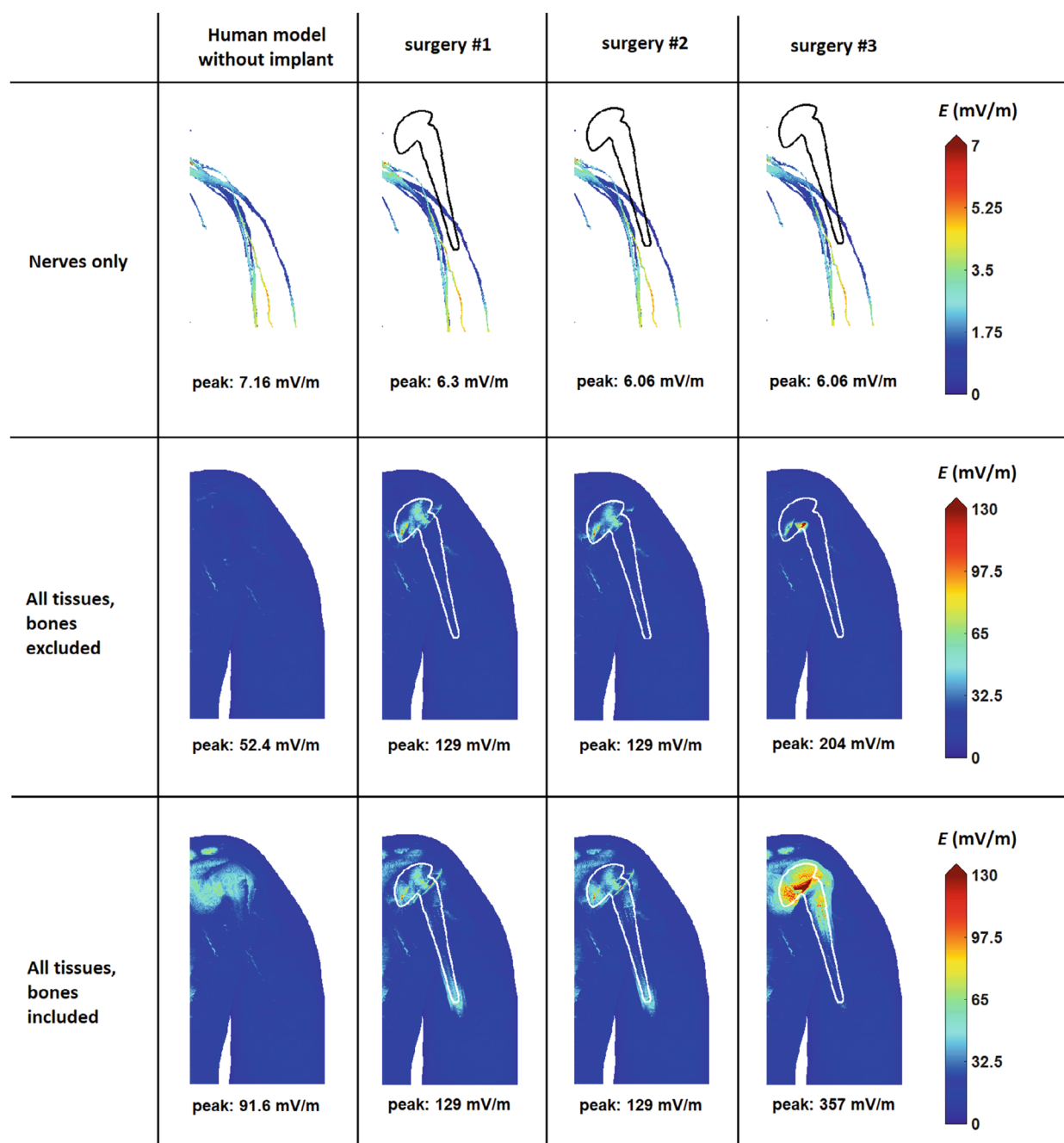


FIGURE 3 Maximum intensity projection (coronal) of the magnitude of the E-field induced in the shoulder region tissues by the X axis of the body gradient coil, during head imaging. Left to right: body model without the implant, surgery 1 (CSF used as a filler), surgery 2 (connective tissue used as a filler), surgery 3 (overlap of the CADs of the body and the implant). Upper row: results in the nerves; middle row: results in all tissues, excluding bones; bottom row: results in all tissues, including bones. The implant is depicted by its footprint. The data refer to a slew rate of 1 (T/m)/s.

the body gradient coil (X axis readout). The maximum intensity projection is reported for the nerve class only, for all tissues excluding bones, and for all tissues including bones. The peak E-field magnitudes in the no-implant model and the models from surgery 1, 2, and 3 are as follows:

- In nerves: 7.16, 6.30, 6.06, 6.06 mV/m

- In tissues, excluding bones: 52.4, 129, 129, 204 mV/m
- In tissues, including bones: 91.6, 129, 129, 357 mV/m.

Given the congruence between the results obtained with surgeries 1 and 2, and considering that surgery 3 is less realistic, section 3.3 will focus on the results of the simulations derived from the model of surgery 1.

TABLE 1 Comparison of the results obtained for a unit slew rate of 1 (T/m)/s in the models without and with the implants (surgery 1), in the body gradient coil, for the shoulder investigation region.

Gradient axis	Imaging target	Peak of E-field without implant (mV/m)	Peak of E-field with implant (mV/m)	Peak ratio R_p	N_e	New peak	Max dB/dt (mT/s)
X	Head	7.16 (52.4) [91.6]	6.30 (129) [129]	0.88 (2.45) [1.40]	0 (401) [25]	No	463
	Thorax	7.03 (40.8) [76.7]	7.20 (44.8) [128]	1.02 (1.10) [1.66]	1 (4) [106]	Yes	301
	Abdomen	6.85 (48.3) [111]	7.15 (136) [136]	1.04 (2.81) [1.22]	1 (1354) [10]	No	463
	Pelvis	7.60 (51.2) [57.5]	7.52 (86.5) [86.5]	0.99 (1.69) [1.50]	0 (38) [67]	No	431
	Femur	1.70 (7.25) [10.2]	1.70 (7.25) [14.0]	1.00 (1.00) [1.37]	1 (1) [195]	Yes	79.2
Y	Head	20.3 (123) [237]	20.4 (128) [240]	1.01 (1.04) [1.01]	3 (1) [1]	No	318
	Thorax	9.12 (71.8) [149]	9.34 (61.3) [150]	1.02 (0.85) [1.01]	2 (0) [1]	No	229
	Abdomen	20.5 (132) [266]	20.7 (137) [269]	1.01 (1.04) [1.01]	3 (1) [1]	No	316
	Pelvis	15.0 (79.3) [142]	15.1 (81.0) [144]	1.00 (1.02) [1.01]	2 (2) [1]	No	268
	Femur	0.791 (5.91) [8.33]	0.791 (5.91) [8.42]	1.00 (1.00) [1.01]	0 (1) [1]	No	35.7
Z	Head	10.8 (61.1) [61.1]	10.9 (62.8) [130]	1.01 (1.03) [2.12]	1 (1) [967]	Yes	381
	Thorax	4.95 (40.3) [62.0]	5.07 (78.0) [78.0]	1.03 (1.93) [1.26]	1 (63) [13]	No	236
	Abdomen	9.49 (67.7) [67.7]	9.52 (80.8) [131]	1.00 (1.19) [1.94]	1 (7) [439]	Yes	379
	Pelvis	7.98 (39.0) [43.2]	7.98 (40.1) [81.8]	1.00 (1.03) [1.89]	0 (1) [657]	Yes	289
	Femur	1.89 (7.88) [10.4]	1.88 (7.87) [11.9]	1.00 (1.00) [1.15]	0 (0) [2]	Yes	45.2

Note: N_e indicates the number of voxels where, when the implant is present, the magnitude of the E-field exceeds the peak value found in the model without the implant (the size of each voxel is 0.5 mm × 0.5 mm × 0.5 mm). Column “New peak” indicates if the presence of the implant creates a new concentration of E-field that was not present in the model without the implant. The values refer to the nerve class only, to all tissues with the exception of the bones (values between round brackets), and to all tissues including the bones (values between square brackets).

Abbreviations: E-field, electric field; max dB/dt, maximum time derivative of the magnetic flux density; N_e , number of voxels; R_p , ratio between the two peak values.

3.3 | Effect of implant, gradient axis, and body position

The results calculated for the body gradient coil are summarized in Tables 1–3 for the shoulder, hip, and knee implants, respectively. Table 4 provides the same comparison for the head gradient coil but references to the shoulder implant and the head imaging position only. All results are based on a slew rate of 1 (T/m)/s.

From this point forward, each configuration will be denoted using a specific code. For example, *shoulder/body-X/head* indicates the results obtained in the shoulder region, when the readout is performed by the X axis of the body gradient coil, during head imaging.

Each table reports the maximum peak of the E-field magnitude induced in the nerves within the investigation region both in the absence and in the presence of the implant. The location of the peak calculated in the two cases in general may be different. Additionally, the tables provide the ratio between the two peak values (with/without implants), indicated as R_p , and the number of voxels (N_e) in which the E-field magnitude computed in

the presence of the implant exceeds the peak computed without the implant. The same quantities, determined by extending the analysis to all tissues except for the bones, are indicated in round brackets. The quantities determined for all tissues including bones are given in square brackets. A “New peak” column indicates instances where the presence of the prosthesis gives rise to a new E-field concentration within the area of consideration.

For the body gradient coil, the strongest increase of the E-field magnitude induced in the nerves is obtained in the *knee/body-Y/abdomen* setup, where the primary peak increases from 7.47 mV/m to 9.25 mV/m ($R_p = 1.24$, $N_e = 40$). A similar amplification is noted in the *knee/Z-body/head* setup, albeit for a significantly weaker field intensity. In the nerves of the shoulder and hip regions, the R_p value is always notably close to (or lower than) 1. In the cases that produce, for each region, the highest peaks of the E-field magnitude (~25 mV/m in *hip/body-Y/thorax* and *hip/body-Y/femur*, ~20 mV/m in *shoulder/body-Y/abdomen* and *shoulder/body-Y/head*, and ~14 mV/m in *knee/body-Y/pelvis*), the field magnitude amplification is always negligible. For the head gradient

TABLE 2 Comparison of the results obtained for a unit slew rate of 1 (T/m)/s in the models without and with the implants (surgery 1), in the body gradient coil, for the hip investigation region.

Gradient axis	Imaging target	Peak of E-field without implant (mV/m)	Peak of E-field with implant (mV/m)	Peak ratio R_p	N_e	New peak	Max dB/dt (mT/s)
X	Head	4.66 (23.2) [44.9]	4.59 (22.8) [43.6]	0.98 (0.98) [0.97]	0 (0) [0]	No	111
	Thorax	19.9 (53.8) [165]	19.7 (85.3) [160]	0.99 (1.59) [0.97]	0 (10) [0]	No	373
	Abdomen	15.4 (51.3) [74.1]	14.1 (49.8) [117]	0.92 (0.97) [1.58]	0 (0) [49]	Yes	366
	Pelvis	12.2 (64.1) [112]	12.0 (63.1) [108]	0.98 (0.98) [0.96]	0 (0) [0]	No	250
	Femur	19.9 (53.8) [165]	20.0 (86.1) [160]	0.99 (1.60) [0.97]	0 (10) [0]	No	374
Y	Head	5.46 (16.9) [42.5]	5.08 (27.5) [55.7]	0.93 (1.63) [1.31]	0 (13) [168]	No	62.6
	Thorax	25.9 (107) [224]	23.9 (143) [356]	0.92 (1.34) [1.59]	0 (4) [108]	Yes	297
	Abdomen	13.7 (48.0) [94.0]	13.0 (62.0) [255]	0.95 (1.29) [2.71]	0 (4) [2927]	Yes	285
	Pelvis	15.1 (45.8) [93.6]	13.7 (67.6) [137]	0.91 (1.48) [1.47]	0 (10) [1431]	No	179
	Femur	25.8 (107) [224]	23.8 (143) [354]	0.92 (1.34) [1.58]	0 (4) [108]	Yes	297
Z	Head	4.17 (20.7) [36.8]	3.91 (20.2) [36.1]	0.94 (0.98) [0.98]	0 (0) [0]	No	71.6
	Thorax	23.0 (96.5) [181]	21.5 (94.7) [174]	0.94 (0.98) [0.96]	0 (0) [0]	No	323
	Abdomen	14.6 (36.8) [76.3]	14.4 (37.9) [74.1]	0.99 (1.03) [0.97]	0 (2) [0]	No	315
	Pelvis	6.26 (34.7) [58.1]	5.76 (34.0) [57.1]	0.92 (0.98) [0.98]	0 (0) [0]	No	182
	Femur	23.1 (96.5) [182]	21.6 (94.7) [175]	0.94 (0.98) [0.96]	0 (0) [0]	No	323

Note: N_e indicates the number of voxels where, when the implant is present, the magnitude of the E-field exceeds the peak value found in the model without the implant (the size of each voxel is 0.5 mm × 0.5 mm × 0.5 mm). Column “New peak” indicates if the presence of the implant creates a new concentration of E-field that was not present in the model without the implant. The values refer to the nerve class only, to all tissues with the exception of the bones (values between round brackets) and to all tissues including the bones (values between square brackets).

Abbreviations: E-field, electric field; max dB/dt, maximum time derivative of the magnetic flux density; N_e , number of voxels; R_p , ratio between the two peak values.

TABLE 3 Comparison of the results obtained for a unit slew rate of 1 (T/m)/s in the models without and with the implants (surgery 1), in the body gradient coil, for the knee investigation region.

Gradient axis	Imaging target	Peak of E-field without implant (mV/m)	Peak of E-field with implant (mV/m)	Peak ratio R_p	N_e	New peak	Max dB/dt (mT/s)
X	Head	0.322 (1.25) [3.85]	0.338 (3.28) [4.40]	1.04 (2.62) [1.14]	4 (2711) [26]	No	9.47
	Thorax	0.711 (7.00) [7.69]	0.739 (8.90) [8.90]	1.04 (1.27) [1.16]	3 (4) [4]	Yes	95.3
	Abdomen	8.62 (32.0) [91.1]	8.98 (79.8) [105]	1.04 (2.49) [1.15]	3 (2034) [33]	No	319
	Pelvis	10.6 (48.2) [160]	12.1 (125) [175]	1.14 (2.60) [1.09]	11 (3299) [11]	No	336
	Femur	7.09 (24.8) [60.4]	7.48 (79.8) [79.8]	1.06 (3.21) [1.32]	2 (266) [3]	Yes	288
Y	Head	0.352 (1.30) [2.77]	0.411 (3.36) [3.36]	1.17 (2.60) [1.21]	27 (1426) [7]	Yes	8.73
	Thorax	1.19 (5.87) [7.85]	1.16 (6.93) [7.54]	0.97 (1.18) [0.96]	0 (5) [0]	No	53
	Abdomen	7.47 (30.5) [64.4]	9.25 (72.4) [72.4]	1.24 (2.37) [1.13]	40 (1136) [6]	No	239
	Pelvis	13.8 (50.3) [93.2]	14.7 (143) [143]	1.06 (2.84) [1.53]	9 (916) [10]	Yes	275
	Femur	7.83 (33.0) [44.6]	7.89 (65.5) [65.5]	1.01 (1.99) [1.47]	1 (60) [5]	Yes	240
Z	Head	0.0935 (0.703) [1.29]	0.116 (1.51) [2.01]	1.24 (2.15) [1.56]	92 (426) [40]	Yes	5.91
	Thorax	1.19 (8.08) [13.9]	1.33 (14.5) [19.0]	1.12 (1.79) [1.37]	22 (155) [21]	Yes	67.2
	Abdomen	3.77 (23.4) [48.4]	4.57 (60.4) [79.5]	1.21 (2.58) [1.64]	53 (1623) [57]	Yes	241
	Pelvis	9.35 (24.3) [75.4]	10.6 (112) [151]	1.14 (4.60) [2.01]	3 (33861) [131]	Yes	291
	Femur	4.36 (23.7) [43.2]	5.08 (44.3) [65.7]	1.17 (1.87) [1.52]	6 (205) [31]	Yes	245

Note: N_e indicates the number of voxels where, when the implant is present, the magnitude of the E-field exceeds the peak value found in the model without the implant (the size of each voxel is 0.5 mm × 0.5 mm × 0.5 mm). Column “New peak” indicates if the presence of the implant creates a new concentration of E-field that was not present in the model without the implant. The values refer to the nerve class only, to all tissues with the exception of the bones (values between round brackets) and to all tissues including the bones (values between square brackets).

Abbreviations: E-field, electric field; max dB/dt, maximum time derivative of the magnetic flux density; N_e , number of voxels; R_p , ratio between the two peak values.

TABLE 4 Comparison of the results obtained for a unit slew rate of 1 (T/m)/s in the models without and with the implants (surgery 1), in the head gradient coil, for the shoulder investigation region.

Imaging target	Gradient axis	Peak of E-field without implant (mV/m)	Peak of E-field with implant (mV/m)	Peak ratio R_p	N_e	New peak	Max dB/dt (mT/s)
Head	X	1.20 (8.24) [22.1]	1.25 (21.2) [29.0]	1.05 (2.57) [1.32]	2 (1673) [4]	Yes	131
	Y	1.83 (12.7) [26.0]	1.96 (13.4) [26.4]	1.07 (1.05) [1.02]	7 (1) [1]	No	55.4
	Z	3.94 (35.3) [48.4]	4.48 (64.7) [64.7]	1.14 (1.83) [1.34]	5 (52) [25]	No	436

Note: N_e indicates the number of voxels where, when the implant is present, the magnitude of the E-field exceeds the peak values found in the model without the implant (the size of each voxel is 0.5 mm \times 0.5 mm \times 0.5 mm). Column “New peak” indicates if the presence of the implant creates a new concentration of E-field that was not present in the model without the implant. The values refer to the nerve class only, to all tissues with the exception of the bones (values between round brackets) and to all tissues including the bones (values between square brackets).

Abbreviations: E-field, electric field; max dB/dt , maximum time derivative of the magnetic flux density; N_e , number of voxels; R_p , ratio between the two peak values.

coil, the strongest E-field amplification in the nerves of the shoulder region is produced by the Z axis ($R_p = 1.14$). This axis also results in the highest E-field peak in the nerves (3.94 mV/m and 4.48 mV/m without and with the implant, respectively).

When the analysis is extended to all tissues excluding bones, pronounced amplifications are observed around the knee implant for almost all scan configurations. The strongest amplification occurs in the *knee/body-Z/pelvis* configuration, where the E-field peak increases from 24.3 mV/m to 112 mV/m ($R_p = 4.60$, $N_e = 33\,861$). Some configurations also show notable amplifications near the hip and shoulder implants, including those involving the head gradient coil.

If the analysis includes bone tissues, some amplification is observed for all implants. The strongest increase is seen in the *hip/body-Y/abdomen* setup, where the peak of the E-field increases from 94 mV/m to 255 mV/m ($R_p = 2.71$, $N_e = 2927$).

We point out that R_p and N_e were determined individually for each set of results (in the nerves, or in the tissues excluding the bones, or in all tissues together). Consequently, when considering all tissues including bones, the values of R_p and N_e may be smaller compared to those derived by excluding the bones. Generally, E-field peaks occurring within the nerves are approximately one order of magnitude lower than the peaks observed when all tissues are included in the analysis. Typically, the highest E-field peaks manifest within the bones, apart from a few exceptions in skin or fat. However, whenever bones are excluded from the simulation, peaks predominantly arise within the skin and fat.

In addition to the data related to the E-field, the tables report the maximum value of the time derivative of the magnetic flux density (max dB/dt) produced in the region of investigation. For the body gradient coil, the highest values are generated by the X axis in all investigation regions. With a 1 (T/m)/s slew rate, these values are

463 mT/s in the shoulder region (*shoulder/body-X/head* and *shoulder/body-X/abdomen*), 374 mT/s in the hip region (*hip/body-X/femur*), and 336 mT/s in the knee region (*knee/body-X/pelvis*). For the head gradient coil, the max dB/dt in the shoulder region is produced by the Z axis, and its value is comparable to the maximum generated by the body gradient coil (436 mT/s).

A visual inspection of the results, for a selection of the investigated configurations, is provided in Figures 4–6. The figures show the maximum intensity projection (on a coronal plane) of the E-field magnitude induced in the nerves and in all tissues (excluding and including bones in the analysis), comparing models without and with implants. Figure 4 reports the case in which R_p is maximized in the nerves (*knee/body-Y/abdomen*, $R_p = 1.24$). Figure 5 reports the case in which R_p is maximized in the tissues, ignoring the bones (*knee/body-Z/pelvis*, $R_p = 4.60$). Figure 6 reports the case in which R_p is maximized in the tissues, including the bones (*hip/body-Y/abdomen*, $R_p = 2.71$). To provide a comprehensive overview, these figures present the results across all gradient axes. In the reported cases, the knee implant tends to concentrate the E-field in the upper part of the knee, whereas the hip implant tends to concentrate the E-field around the stem of the prosthesis.

4 | DISCUSSION

4.1 | The role of the slew rate and of the virtual surgery

As indicated in section 3.1, we have verified the scaling law of the results when implants are present. This means that there is a directly proportional relationship between the slew rate and the amplitude of the E-field induced in tissues. This was tested up to a slew rate of 400 (T/m)/s for selected cases. Notably, this outcome could not be assumed

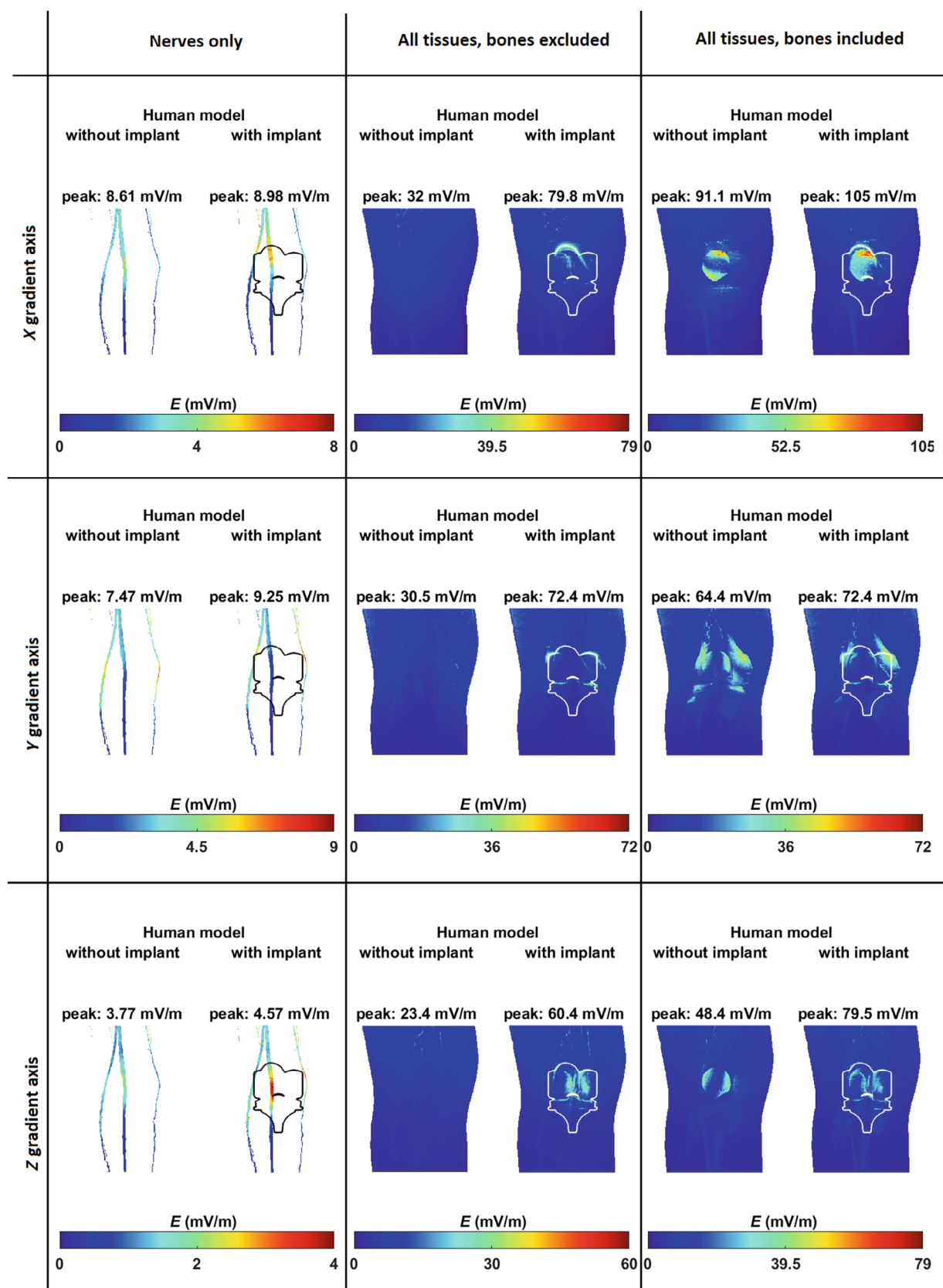


FIGURE 4 Maximum intensity projection (coronal) of the magnitude of the E-field induced in the knee region tissues by the X axis (upper row), Y axis (middle row), and Z axis (bottom row) of the body gradient coil, during abdominal imaging. First column: results in the nerves only; second column: results in all tissues, excluding bones; third column: results in all tissues, including bones. The implant is depicted by its footprint. The data refer to a slew rate of 1 (T/m)/s.

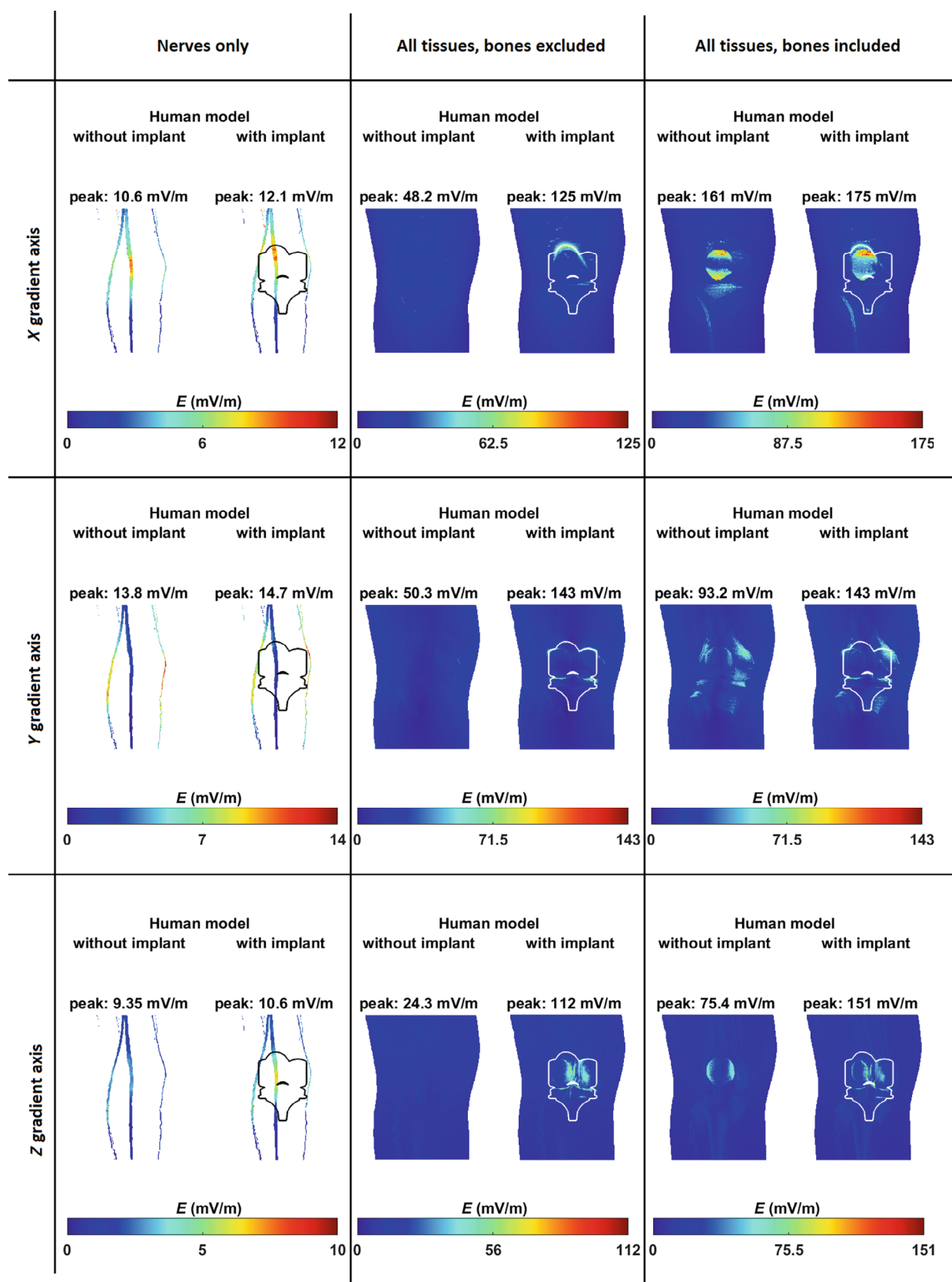


FIGURE 5 Maximum intensity projection (coronal) of the magnitude of the E-field induced in the knee region tissues by the X axis (upper row), Y axis (middle row), and Z axis (bottom row) of the body gradient coil, during pelvic imaging. First column: results in the nerves only; second column: results in all tissues, excluding bones; third column: results in all tissues, including bones. The implant is depicted by its footprint. The data refer to a slew rate of 1 (T/m)/s.

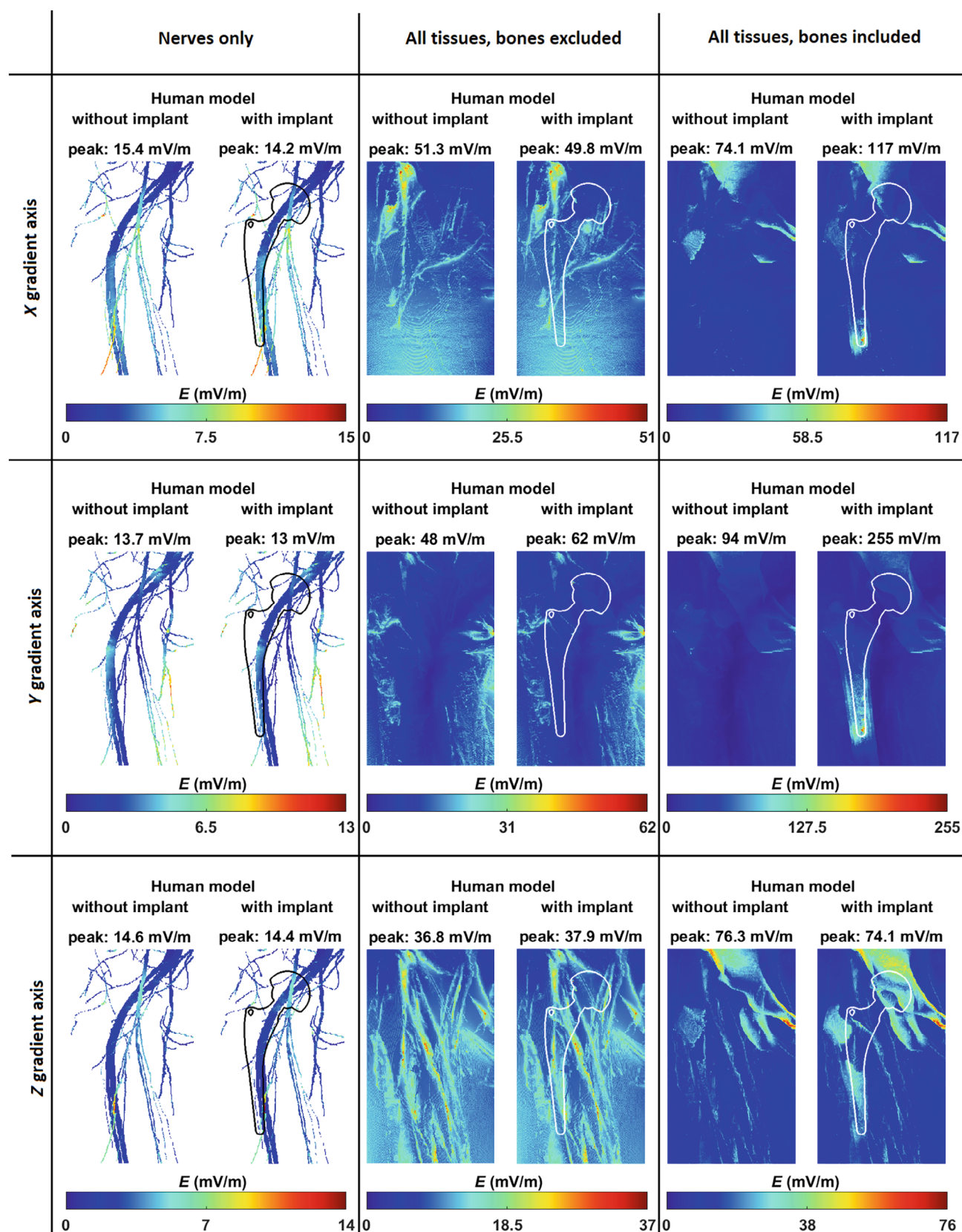


FIGURE 6 Maximum intensity projection (coronal) of the magnitude of the E-field induced in the hip region tissues by the X axis (upper row), Y axis (middle row), and Z axis (bottom row) of the body gradient coil, during abdominal imaging. First column: results in the nerves only; second column: results in all tissues, excluding bones; third column: results in all tissues, including bones. The implant is depicted by its footprint. The data refer to a slew rate of 1 (T/m)/s.

a priori due to the perturbing effect of the eddy currents induced in the metallic parts. However, this finding simplifies our analysis. It means that we can estimate E-field magnitudes for any slew rate (at least up to 400 (T/m)/s) through simple linear scaling.

Concerning the different versions of the body model with prostheses, the induced E-fields are consistent between models 1 and 2. This is despite the different values of electrical conductivity adopted for the material that fills the void made during the virtual surgery (1.78 S/m compared to 0.37 S/m). This consistency arises because, for all prosthetic models, the filler is surrounded by fat, which has a much lower conductivity (0.057 S/m). Thus, the choice of the conductivity assigned to the filler has a weak influence on the result, provided that it is substantially higher than the conductivity of fat. However, no void was created in surgery 3, where a simple overlap between the CADs of the body and the implants was performed. This means the model includes some unrealistic residual of the original bones, and these remnants have a conductivity similar to the conductivity of the surrounding fat. The electromagnetic behavior of surgery 3 therefore deviates from the behavior of surgeries 1 and 2. Given that the local distribution of the E-field can substantially impact PNS, these results underline the importance of modeling orthopedic surgeries in an accurate way. Conversely, uncertainties regarding the choice of filler conductivity have a lesser impact.

4.2 | Field distribution in the model without implants

For the human model without implants, some preliminary discussions and comparisons with previously published investigations are possible.

Despite the use of different coils and body models, our results, when adjusted for slew rate, align well with recent comparable calculations.²⁸ Notably, echoing reports from other authors,³⁸ the highest peaks of E-field magnitude are produced by the Y axis of the body gradient coil. This is observed both in the hip region (when imaging the thorax or the femur) and in the shoulder region (when the abdomen is the target of the MRI exam, although strong values also arise for other scan positions).

When, at the same slew rate, the head gradient coil is used to image the patient's head, the E-field induced in the shoulder region is weaker with respect to the field obtained with the body gradient coil. This is in line with previous analyses,³³ which have highlighted how coils of this kind have a higher PNS threshold (by virtue of their reduced size) with respect to body gradient coils. For the head gradient coil, the Z axis induces the strongest E-field

in the shoulder region. Interestingly, previous investigations found that the Z axis tends to present the lowest PNS threshold in the shoulder when associated with head gradient coils.^{39,40}

Previous experimental investigations⁴¹ found a poor correlation between the location of the max dB/dt and the location of the PNS perception. With the body gradient coil, the present analysis indicates that, in general, the highest dB/dt values do not correspond to the strongest E-field peaks. With the head gradient coil, the max dB/dt in the shoulder region is produced by the Z axis (which also produces the strongest E-field). Its value is comparable to the max dB/dt produced by the body gradient coil; however, as previously mentioned, the peaks of the E-field magnitude are lower.

4.3 | Effect of the implants

The results put in evidence that, in some cases, the presence of bulky metallic implants may produce a significant perturbation in the distribution of the induced E-field. If, to some extent, this outcome was predictable, the proposed analysis shows such an effect in quantitative terms, identifying the anatomical points where it takes place. Concerning this, in about one half of the investigated cases, new peaks of the induced E-field originate from the introduction of the implants in the investigated regions.

Recent investigations based on neurodynamic models²⁸ have identified the primary subbranches of the major nerves (which exhibit relatively large diameters, combined with sharp kinks) as main candidates for the stimulation. Therefore, a prominent position has been given to the analysis of the E-field in the nerves of the human model. Focusing the attention on the nerve class, significant amplifications of the E-field magnitude are observed for the knee implant only. Arguably, considering that significant amplifications are observed also in the other tissues surrounding this prosthesis, the presence of the knee implant creates conditions that may facilitate PNS, lowering the threshold for the onset of the stimulation in this part of the body.

In the main motor nerves that surround the shoulder and hip implant, the amplification of the E-field is always feeble. However, if the analysis is extended to all tissues, it becomes significant, in many cases, also around these prostheses. This situation is well illustrated by Figures 4–6, which show that the amplification of the E-field peaks produced by the implants changes significantly based on the group of tissues included in the analysis. If, on the one hand, this outcome complicates the interpretation of the results, on the other hand it suggests that the effect of implants on PNS is worth deepening. Indeed, the amplification of the E-field is not detected exclusively

in the bone voxels (which are in direct contact with the implants but should give a minor contribution to PNS due to the paucity of motor nerves). Significant amplifications have been also observed in the voxels assigned to other tissues (in particular in skin and fat), which are accounted for in traditional dosimetric assessments of PNS.²⁹ Hence, because smaller nerves may be “hidden” within voxels assigned to other tissues, the magnitude of the E-field induced in the other materials around the implants has been considered as well. Interestingly, a good correlation has been found between parameters R_p and N_e (see Tables 1–4). For instance, the highest amplification observed in the analysis that involves all tissues except the bones occurs in *knee/body-Z/pelvis* ($R_p = 4.60$). This is also the case in which the largest N_e value has been obtained ($N_e = 33\,861$). This coincidence corroborates the idea that the E-field amplification may involve nerves that are not represented in the adopted human model.

In principle, based on the value of parameter R_p , the following rationale could be formulated to identify potentially risky situations. If a given MRI exam does not produce PNS in the absence of implants, it is reasonable to assume that the same exam can be safely applied to a patient bearing an implant, provided that the corresponding value of R_p is close to (or lower than) 1. This is particularly true if the introduction of the implant does not produce a significant modification of the spatial pattern of the induced E-field, and conversely, cases in which $R_p > 1$ would require a note of caution (especially if the value of N_e is relatively large) because the increase of the E-field could trigger the PNS sensation. Nevertheless, this kind of analysis would not be feasible in clinical practice, where more general rules are required. Indeed, at the state of the art, the MRI scanners do not perform any patient-specific assessment of PNS but rely on general safety measures. According to the International Electrotechnical Commission standards,¹ the scanners shall be designed to minimize the occurrence of PNS in normal operating mode. This condition is obtained by limiting the gradient output (e.g., the time derivative of the gradient field in the volume taken up by the patient’s body) below suitable reference values (80% of the conventional PNS threshold, in normal operating mode). The latter were deduced from calculations and experimental investigations and did not consider the possible presence of an implant inside the body. Because the proposed analysis indicates that the presence of bulky implants may change the E-field distribution and amplify its magnitude, new investigations would be desirable to check whether condition $R_p > 1$ (that is not dangerous per se) turns out to be really associated with an increased PNS risk. Such investigations should clarify whether the presence of an implant in one side of the body reduces the PNS threshold with respect to the other side of

the same body, where the implant is not present. Moreover, the investigations should assess whether the variation of the PNS threshold ascribed to the implants is significant with respect to the intersubject variation observed in the absence of implants. If needed, suitable limits could be formulated for patients carrying implants and the standards could be updated accordingly. To mitigate the increase of the E-field magnitude during the MRI exam, two strategies could be applied: a reduction of the slew rate, and an optimal choice of the gradient axis that performs the read-out. To be feasible in clinical practice, both strategies shall comply with imaging requirements.

4.4 | Limitations

When using the results of our proposed analysis to evaluate the increase in the risk of PNS in the presence of an implant, some limitations must be considered. From the technical viewpoint, the calculated E-field values may be affected by the so-called staircasing artifacts (especially at tissue interfaces with strong contrast, in terms of conductivity) and other sources of numerical outliers.⁴² To mitigate these anomalies, the International Commission on Non-Ionizing Radiation Protection guidelines²⁹ recommend the use of the 99th percentile. However, this strategy has been widely questioned⁴³ and, even if other techniques have been proposed in the literature,^{44–46} this issue has not yet been completely settled. Thus, in this paper, the raw results have been provided under the tacit assumption that they must be considered affected by some uncertainty (as always in computational electromagnetic dosimetry). Nevertheless, the good correlation between parameters R_p and N_e can be used to corroborate the trustworthiness in a case that exhibits a significant increase in the E-field.

In terms of the interpretation of the results, the use of the E-field magnitude as a metric to quantify the risk of PNS is the main limitation of the work. Indeed, PNS originates from the interaction between the E-field and the nerves (an interaction that involves their relative spatial orientation), and therefore the stimulation does not necessarily occur where the E-field is stronger but where a good coupling between the E-field and the nerve track takes place. Future investigations based on neurodynamic simulations of a human model carrying implants are therefore seen as the natural development of the present analysis.

As already mentioned, the validity of the linear proportion between the E-field magnitude and the slew rate has been verified up to 400 (T/m)/s. With the continuous development of the technology, higher slew rates might be involved in the clinical practice, requiring an update of this aspect of the investigation.

5 | CONCLUSION

The presence of bulky orthopedic implants can substantially modify the distribution of the E-field induced by gradient coils in the body of a patient undergoing MRI, leading to an appreciable increase in the E-field magnitude. Our proposed analysis has investigated the problem quantitatively, emphasizing a realistic model of orthopedic surgery.

While an increase in the E-field magnitude does not necessarily imply the onset of PNS, the results suggest that subjects carrying orthopedic implants should be included in future experimental surveys aimed at determining PNS thresholds. Parallel to this, the E-field distributions obtained during this study can provide the starting point for further investigations aimed at predicting the onset of PNS events in the presence of implants, through neurodynamic models.

ACKNOWLEDGMENTS

The results presented here have been developed in the framework of the 17IND01 MIMAS Project “Procedures allowing medical implant manufacturers to demonstrate compliance with MRI safety regulations” and 21NRM05 STASIS Project “Standardization for safe implant scanning”. The 17IND01 MIMAS Project has received funding from the EMPIR programme co-financed by the Participating States and from the European Union’s Horizon 2020 research and innovation programme. The 21NRM05 STASIS Project has received funding from the European Partnership on Metrology, cofinanced from the European Union’s Horizon Europe Research and Innovation Programme and by the Participating States. The authors acknowledge the support of Zurich MedTech (Zurich, Switzerland) in the development of the human model with implants. CAD models of hip and knee implants were kindly provided by the manufacturer of prosthetic devices Adler Ortho SpA, Cormanio (MI), Italy (www.adlerortho.com). The authors wish to express thanks to Dr. Rosie Goodburn for the assistance in the preparation of the final paper.

ORCID

Luca Zilberti  <https://orcid.org/0000-0002-2382-4710>

Alessandro Arduino  <https://orcid.org/0000-0002-4829-5130>

Riccardo Torchio  <https://orcid.org/0000-0002-2916-8793>

Umberto Zanovello  <https://orcid.org/0000-0001-6415-9967>

Oriano Bottauscio  <https://orcid.org/0000-0002-5437-4396>

REFERENCES

1. International Electrotechnical Commission (IEC). *IEC 60601-2-33 Medical Electrical Equipment – Part 2-33: Particular Requirements for the Basic Safety and Essential Performance of Magnetic Resonance Equipment for Medical Diagnosis, Edition 4.0*. IEC; 2022.
2. Schaefer DJ, Bourland JD, Nyenhuis JA. Review of patient safety in time-varying gradient fields. *J Magn Reson Imaging*. 2000;12:20-29.
3. Panych LP, Madore B. The physics of MRI safety. *J Magn Reson Imaging*. 2018;47:28-43.
4. Davids M, Guérin B, Klein V, Wald LL. Optimization of MRI gradient coils with explicit peripheral nerve stimulation constraints. *IEEE Trans Med Imaging*. 2021;40:129-142.
5. Roemer PB, Rutt BK. Minimum electric-field gradient coil design: theoretical limits and practical guidelines. *Magn Reson Med*. 2021;86:569-580.
6. Hidalgo-Tobon SS, Bencsik M, Bowtell R. Reducing peripheral nerve stimulation due to gradient switching using an additional uniform field coil. *Magn Reson Med*. 2011;66:1498-1509.
7. Loecher M, Middione MJ, Ennis DB. A gradient optimization toolbox for general purpose time-optimal MRI gradient waveform design. *Magn Reson Med*. 2020;84:3234-3245.
8. In MH, Shu Y, Trzasko JD, et al. Reducing PNS with minimal performance penalties via simple pulse sequence modifications on a high-performance compact 3T scanner. *Phys Med Biol*. 2020;65:15NT02.
9. Schulte RF, Noeske R. Peripheral nerve stimulation-optimal gradient waveform design. *Magn Reson Med*. 2015;74:518-522.
10. Zilberti L, Arduino A, Bottauscio O, Chiampi M. The underestimated role of gradient coils in MRI safety. *Magn Reson Med*. 2017;77:13-15.
11. Brühl R, Ihlenfeld A, Ittermann B. Gradient heating of bulk metallic implants can be a safety concern in MRI. *Magn Reson Med*. 2017;77:1739-1740.
12. Winter L, Seifert F, Zilberti L, Murbach M, Ittermann B. MRI-related heating of implants and devices: a review. *J Magn Reson Imaging*. 2021;53:1646-1665.
13. Arduino A, Zanovello U, Hand J, et al. Heating of hip joint implants in MRI: the combined effect of radiofrequency and switched-gradient fields. *Magn Reson Med*. 2021;85:3447-3462.
14. Wooldridge J, Arduino A, Zilberti L, et al. Gradient coil and radiofrequency induced heating of orthopaedic implants in MRI: influencing factors. *Phys Med Biol*. 2021;66:245024.
15. Arduino A, Bottauscio O, Chiampi M, Zanovello U, Zilberti L. A contribution to MRI safety testing related to gradient-induced heating of medical devices. *Magn Reson Med*. 2022;88:930-944.
16. Clementi V, Zanovello U, Arduino A, et al. Classification scheme of heating risk during MRI scans on patients with orthopaedic prostheses. *Diagnostics*. 2022;12:1873.
17. Bassen H, Zaidi T. Parameters affecting worst-case gradient-field heating of passive conductive implants. *J Magn Reson Imaging*. 2022;56:1197-1204.
18. Reilly JP, Diamant AM. Theoretical evaluation of peripheral nerve stimulation during MRI with an implanted spinal fusion stimulator. *Magn Reson Imaging*. 1997;15:1145-1156.
19. Buechler DN, Durney CH, Christensen DA. Calculation of electric fields induced near metal implants by magnetic resonance

- imaging switched-gradient magnetic fields. *Magn Reson Imaging*. 1997;15:1157-1166.
20. Turk EA, Kopanoglu E, Guney S, et al. A simple analytical expression for the gradient induced potential on active implants during MRI. *IEEE Trans Biomed Eng*. 2012;59:2845-2851.
 21. Chen X, Edmonson J, Steckner M. The potential for Eddy current induced peripheral nerve stimulation from an active implanted device canister. In *Proceedings of the 24th Annual Meeting and Exhibition of ISMRM*. International Society for Magnetic Resonance in Medicine; 2016:p. 2234.
 22. Sawyer-Glover AM, Shellock FG. Pre-MRI procedure screening: recommendations and safety considerations for biomedical implants and devices. *J Magn Reson Imaging*. 2000;12:92-106.
 23. Naraghi AM, White LM. Magnetic resonance imaging of joint replacements. *Semin Musculoskelet Radiol*. 2006;10:98-106.
 24. Hartley KG, Damon BM, Patterson GT, Long JH, Holt GE. MRI techniques: a review and update for the orthopaedic surgeon. *J Am Acad Orthop Surg*. 2012;20:775-787.
 25. Hayter CL, Koff MF, Potter HG. Magnetic resonance imaging of the postoperative hip. *J Magn Reson Imaging*. 2012;35:1013-1025.
 26. Sim4Life. *Computable Human Phantoms*. Zurich MedTech; 2014. <https://zmt.swiss/sim4life/>. Accessed July 19, 2021.
 27. Hasgall PA, Di Gennaro F, Baumgartner C, et al. IT^{IS} Database for Thermal and Electromagnetic Parameters of Biological Tissues, Version 4.0. May 15, 2018. Available at: <https://itis.swiss/virtual-population/tissue-properties/overview/>. Accessed July 19, 2021.
 28. Davids M, Guérin B, vom Endt A, Schad LR, Wald LL. Prediction of peripheral nerve stimulation thresholds of MRI gradient coils using coupled electromagnetic and neurodynamic simulations. *Magn Reson Med*. 2019;81:686-701.
 29. International Commission on Non-Ionizing Radiation Protection (ICNIRP). Guidelines for limiting exposure to time-varying electric and magnetic fields (1–100 kHz). *Health Phys*. 2010;99:818-836.
 30. Fagan AJ, Bitz AK, Björkman-Burtscher IM, et al. 7T MR safety. *J Magn Reson Imaging*. 2021;53:333-346.
 31. Ehrhardt JC, Lin CS, Magnotta VA, Fisher DJ, Yuh WT. Peripheral nerve stimulation in a whole-body echo-planar imaging system. *J Magn Reson Imaging*. 1997;7:405-409.
 32. Den Boer JA, Bourland JD, Nyenhuis JA, et al. Comparison of the threshold for peripheral nerve stimulation during gradient switching in whole body MR systems. *J Magn Reson Imaging*. 2002;15:520-525.
 33. Hennel F, Wilm B, Roesler MB, Weiger M, Dietrich B, Pruessmann KP. Echo-planar imaging of the human head with 100 mT/m gradients and high-order modeling of eddy current fields. *Magn Reson Med*. 2020;84:751-761.
 34. Torchio R, Arduino A, Zilberti L, Bottauscio O. A fast tool for the parametric analysis of human body exposed to LF electromagnetic fields in biomedical applications. *Comput Methods Programs Biomed*. 2021;214:106543.
 35. Milshteyn E, Guryev G, Torrado-Carvajal A, et al. Individualized SAR calculations using computer vision-based MR segmentation and a fast electromagnetic solver. *Magn Reson Med*. 2021;85:429-443.
 36. Bettini P, Torchio R, Lucchini F, Voltolina D, Alotto P. Fast Fourier transform-volume integral: a smart approach for the electromagnetic design of complex systems in large fusion devices. *Plasma Phys Control Fusion*. 2021;63:025010.
 37. Polimeridis AG, Villena JF, Daniel L, White JK. Stable FFT-JVIE solvers for fast analysis of highly inhomogeneous dielectric objects. *J Comput Phys*. 2014;269:280-296.
 38. So PPM, Stuchly MA, Nyenhuis JA. Peripheral nerve stimulation by gradient switching fields in magnetic resonance imaging. *IEEE Trans Biomed Eng*. 2004;51:1907-1914.
 39. Lee SK, Mathieu JB, Graziani D, et al. Peripheral nerve stimulation characteristics of an asymmetric head-only gradient coil compatible with a high-channel-count receiver array. *Magn Reson Med*. 2016;76:1939-1950.
 40. Tan ET, Hua Y, Fiveland EW, et al. Peripheral nerve stimulation limits of a high amplitude and slew rate magnetic field gradient coil for neuroimaging. *Magn Reson Med*. 2020;83:352-366.
 41. Ham CLG, Engels JM, van de Wiel GT, Machiels A. Peripheral nerve stimulation during MRI: effects of high gradient amplitudes and switching rates. *J Magn Reson Imaging*. 1997;7:933-937.
 42. Reilly JP, Hirata A. Low-frequency electrical dosimetry: research agenda of the IEEE international committee on electromagnetic safety. *Phys Med Biol*. 2016;61:R138-R149.
 43. International Commission on Non-Ionizing Radiation Protection (ICNIRP). Gaps in knowledge relevant to the “guidelines for limiting exposure to time-varying electric and magnetic fields (1 Hz–100 kHz)”. *Health Phys*. 2020;118:533-542.
 44. Laakso I, Hirata A. Reducing the staircasing error in computational dosimetry of low-frequency electromagnetic fields. *Phys Med Biol*. 2012;57:N25-N34.
 45. Gomez-Tames J, Laakso I, Haba Y, Hirata A, Poljak D, Yamazaki K. Computational artifacts of the In situ electric field in anatomical models exposed to low-frequency magnetic field. *IEEE Trans Electromagn Compat*. 2018;60:589-597.
 46. Arduino A, Bottauscio O, Chiampi M, et al. Accuracy assessment of numerical dosimetry for the evaluation of human exposure to electric vehicle inductive charging systems. *IEEE Trans Electromagn Compat*. 2020;62:1939-1950.

How to cite this article: Zilberti L, Arduino A, Torchio R, et al. Orthopedic implants affect the electric field induced by switching gradients in MRI. *Magn Reson Med*. 2024;91:398-412. doi: 10.1002/mrm.29861